Journal of Computational Science 92 (2025) 102704

Contents lists available at ScienceDirect

Journal of Computational Science

journal homepage: www.elsevier.com/locate/jocs

Numerical solution of the biological SIR model for COVID-19 with convergence analysis

Walid Remili [a,*], Wen-Xiu Ma [b,c,d,e,*]

[a] Faculty of Mathematics and Computer Science, University of M'sila, PO Box 166, Ichebilia, 28000 M'sila, Algeria
[b] Department of Mathematics, Zhejiang Normal University, Jinhua, Zhejiang 321004, PR China
[c] Research Center of Astrophysics and Cosmology, Khazar University, 41 Mehseti Street, Baku 1096, Azerbaijan
[d] Department of Mathematics and Statistics, University of South Florida, Tampa, FL 33620-5700, USA
[e] Material Science Innovation and Modeling, North-West University, Mafikeng Campus, Mmabatho 2735, South Africa

ARTICLE INFO

MSC:
45B05
34B15
33C45
65R20

Keywords:
Biological Susceptible–Infectious–Recovered model
Volterra integral equation
Shifted Chebyshev polynomials
Collocation method

ABSTRACT

This study investigates the numerical solution of the biological Susceptible–Infectious–Recovered model for COVID-19 over extended time intervals using the shifted Chebyshev polynomial collocation method. Initially, the original problem is reformulated into a nonlinear Volterra integral equation for the susceptible population. The shifted Chebyshev polynomials are then employed to derive the numerical solution. A comprehensive convergence analysis of the collocation method is conducted to ensure the reliability and accuracy of the proposed approach. Finally, numerical simulations are performed for various parameter configurations that influence the system's coefficients. Our method is compared with existing approaches, providing insights into the model's dynamics under different conditions.

1. Introduction

COVID-19 is a member of the Coronaviridae family, which primarily affects the respiratory system. The epidemic dynamics of COVID-19 are often modeled using the Susceptible–Infectious–Recovered (SIR) model, a well-established framework in epidemiology (see [1] and references therein). The SIR model has also been applied to study the spread of other infectious diseases, such as influenza and Ebola, as demonstrated by Earn et al. [2] and Khaleque & Sen [3]. The SIR model was initially proposed by Kermack and McKendrick [4] and is described by the following system of ordinary differential equations:

$$\begin{aligned} S'(t) &= -\alpha S(t)I(t), & S(0) &= \tilde{s}_0, \\ I'(t) &= \alpha S(t)I(t) - \beta I(t), & I(0) &= \tilde{i}_0, \\ R'(t) &= \beta I(t), & R(0) &= \tilde{r}_0, \end{aligned} \tag{1}$$

with the constraint

$$S(t) + I(t) + R(t) = N,$$

where:

- $S(t)$ represents the susceptible population (individuals who are at risk of contracting the disease),
- $I(t)$ represents the infected population (individuals currently infected with the disease),
- $R(t)$ represents the recovered population (individuals who have recovered from the disease and are assumed to be immune),
- N is the total population in the region under consideration.

The coefficients in the model are defined as follows:

- α is the infection rate, which determines how quickly susceptible individuals become infected upon contact with infectious individuals,
- β is the recovery rate, which represents the rate at which infected individuals recover from the disease.

Over the past years, the analytical and approximate solutions of the SIR model have been extensively studied by various authors. For analytical studies, Harko et al. [5] were the first to derive exact analytical solutions, presenting them in an exact parametric form. Additionally, the analytical solutions discussed by Barlow & Weinstein [6] and Prodanov [7] are expressed in terms of the Lambert W function, with Prodanov [7] also providing a numerical solution. For semi-analytical approaches, Makinde [8] employed the Adomian

* Corresponding authors.
E-mail addresses: walid.remili@univ-msila.dz (W. Remili), mawx@cas.usf.edu (W.-X. Ma).

https://doi.org/10.1016/j.jocs.2025.102704
Received 13 June 2025; Received in revised form 3 August 2025; Accepted 18 August 2025
Available online 17 September 2025

decomposition method, while Chakir [9] proposed the Padé approximation method. In the context of numerical solutions, Piyawong et al. [10] introduced a first-order finite-difference scheme to explicitly obtain numerical solutions. Furthermore, Conte et al. [11] and Mickens [12] developed nonstandard finite-difference schemes capable of preserving the positivity of the exact solution. A collocation scheme based on Hermite wavelets was presented by Baleanu et al. [13], and Kumar [14] proposed a Taylor wavelets collocation technique. Very recently, Khoa et al. [15] reformulated the system of differential equations defined in (1) as follows:

$$\begin{cases} R'(t) = \beta(N - \tilde{s}_0 e^{-\mu R(t)} - R(t)), \quad \mu = \dfrac{\alpha}{\beta}, \quad t \in \Omega_T = [0, T], \quad T \in \mathbb{R}^+, \\ S(t) = \tilde{s}_0 e^{-\mu R(t)}, \\ I(t) = (N - \tilde{s}_0 e^{-\mu R(t)} - R(t)), \\ I_{\max} = -\dfrac{1}{\mu}\ln(\mu) + \tilde{i}_0 + \tilde{s}_0 - \dfrac{1}{\mu}\ln(\tilde{s}_0). \end{cases} \tag{2}$$

Khoa et al. proved the existence of a unique solution of the problem (2) in the space of continuous functions and obtained the numerical solution using an efficient relaxation scheme. They also provided a convergence analysis based on the infinity norm.

In general, obtaining a theoretical convergence analysis for the system (1) is not straightforward. Therefore, the aim of this paper is to introduce and analyze a new superconvergent postprocessing technique for the system (1). To this end, the problem in (2) can be equivalently expressed as a nonlinear Volterra integral equation:

$$R(t) = \tilde{r}_0 + \int_0^t k(s, R(s))\, ds, \quad t \in \Omega_T, \tag{3}$$

where $k(t, R(t)) = \beta\left(N - \tilde{s}_0 e^{-\mu R(t)} - R(t)\right)$. To ensure the unique solvability of (3), we establish that the kernel k satisfies a Lipschitz condition in R. This is based on the Lipschitz continuity of the exponential function $e^{-\mu t}$ follows from the mean value theorem, as $|\frac{d}{dt}e^{-\mu t}| = \mu e^{-\mu t} \le \mu$ for $t \ge 0$, ensuring $|e^{-\mu S} - e^{-\mu R}| \le \mu|S - R|$. Hence, for any $S, R \in \mathbb{R}^+$, we have:

$$|k(t, S) - k(t, R)| \le \beta(\mu\tilde{s}_0 + 1)|S - R|. \tag{4}$$

Thus, k is globally Lipschitz continuous in R with constant $L = \beta(\mu\tilde{s}_0 + 1)$. To solve Eq. (3), we employ shifted Chebyshev polynomials (SCPs), which are mutually orthogonal in the weighted L^2-space. These polynomials are derived from the classical third-kind Chebyshev polynomials (TKCP) via a suitable change of variable. We further establish the convergence analysis for the approximate solutions, yielding an error of order $\mathcal{O}(N^{\frac{1}{2}-m})$. The primary advantage of SCPs lies in their ability to achieve superconvergence over small intervals while maintaining high accuracy for large intervals. This property makes them particularly effective for solving differential and integral equations, especially in epidemiological modeling. Several recent studies have demonstrated the efficacy and versatility of Chebyshev-based spectral and collocation methods in solving diverse classes of fractional and integer-order differential equations. For instance, Srivastava et al. [16] employed Chebyshev polynomials to develop an efficient spectral collocation method for simulating the dynamics of a fractional SIRD model describing the Ebola virus. Similarly, Sriwastav et al. [17] proposed a novel collocation scheme based on shifted Chebyshev polynomials to address a class of three-point singular boundary value problems. Sayed et al. [18] introduced a spectral framework using modified shifted Chebyshev polynomials of the third kind for solving one- and two-dimensional hyperbolic telegraph equations. Abdelhakem et al. [19] developed two modified shifted Chebyshev–Galerkin methods tailored to even-order partial boundary value problems. In the context of nonlinear fractional differential equations, Youssri and Atta [20] proposed an explicit collocation algorithm using third-kind Chebyshev polynomials to solve the nonlinear fractional Duffing equation. Additionally, Youssri et al. [21] presented a spectral collocation approach employing first-kind Chebyshev polynomials for the time-fractional Korteweg–de Vries–Burgers equation. Further advancing this area, Youssri and Atta [22] introduced an adopted Chebyshev collocation method for modeling the human corneal shape via the Caputo fractional derivative. Moreover, the Chebyshev Petrov–Galerkin method was developed by the same authors [23] to handle nonlinear time-fractional integro-differential equations featuring mildly singular kernels. Beyond Chebyshev-based approaches, additional advanced numerical techniques have also been explored. Sriwastav et al. [24] proposed a meshfree method combining spline-based multistage Bernstein collocation to model rennet-induced coagulation equations. Pathak et al. [25] formulated an algorithm grounded in homotopy perturbation theory for solving singular nonlinear boundary value problems. For applications in stellar physics, Sriwastav et al. [26] devised a robust Legendre collocation scheme tailored to Lane–Emden multi-pantograph delay differential equations, including those modeling Chandrasekhar's white dwarf problem. Additional contributions include the Haar wavelet collocation method introduced by Singh, Garg, and Guleria [27] for Lane–Emden equations, and the Taylor operational matrix method proposed by Saha and Singh [28] for solving third-order Emden–Fowler-type pantograph equations. Lastly, Shahni et al. [29] presented an efficient numerical method for three-point Lane–Emden–Fowler boundary value problems.

The remainder of this paper is organized as follows. In Section 2, we introduce the required integral operator, review some basic concepts related to the TKCPs, and present the SCPs. In Section 3, we discuss the numerical solution of Eq. (3). Section 4 presents the convergence results of the collocation method in the standard L^∞-space. Finally, Section 5 presents a series of numerical experiments to validate the effectiveness of the proposed technique, including direct comparisons with existing methods. To further illustrate the robustness and accuracy of our approach, several numerical simulations are provided throughout the paper. These simulations not only yield quantitative assessments but also offer visual insights into the dynamic progression of the COVID-19 outbreak. In particular, the figures and numerical simulations underscore the capability of the proposed method to accurately capture key epidemiological features such as the infection peak and recovery trends—elements that are essential in understanding and managing epidemic dynamics. The paper concludes with Section 6, where we summarize the findings and present the conclusions.

2. Theoretical framework

Let $\mathbb{X} = L^\infty(\Omega_T)$ be a Banach space. From Theorem 1 in [15], the system (2) admits unique positive solutions S^*, I^*, and R^* in $C^1(\Omega_T)$. Consequently, the solution R^* can be expressed as:

$$R^*(t) = \tilde{r}_0 + \int_0^t k(s, R^*(s))\, ds, \quad t \in \Omega_T,$$

with

$$S^*(t) = \tilde{s}_0 e^{-\mu R^*(t)}, \tag{5}$$

$$I^*(x) = (N - \tilde{s}_0 e^{-\mu R^*(t)} - R^*(t)). \tag{6}$$

To analyze this further, we define the integral operator $\mathcal{K} : \mathbb{X} \to \mathbb{X}$ as follows:

$$\mathcal{K}(R)(t) = \int_0^t k(s, R(s))\, ds, \quad t \in \Omega_T, \tag{7}$$

where

$$k(t, R(t)) = \beta\left(N - \tilde{s}_0 e^{-\mu R(t)} - R(t)\right).$$

Using this operator, Eq. (3) can be rewritten as:

$$R(t) - \mathcal{K}(R)(t) = \tilde{r}_0, \quad t \in \Omega_T.$$

For any $R, S \in \mathbb{X}$ and from (4), the difference $\mathcal{K}(R) - \mathcal{K}(S)$ satisfies:

$$|\mathcal{K}(R)(t) - \mathcal{K}(S)(t)| \le \beta\left(\tilde{s}_0\mu + 1\right) t \|S - R\|_\infty. \tag{8}$$

Taking the supremum over $t \in \Omega_T$, we obtain:

$$\|\mathcal{K}(R) - \mathcal{K}(S)\|_\infty \leq \beta \left(\tilde{s}_0\mu + 1\right) T \|S - R\|_\infty. \tag{9}$$

Next, we introduce the Fréchet derivative of the nonlinear operator $\mathcal{K}$ at R^*, denoted by $\mathcal{K}'(R^*)$. For $w \in \mathbb{X}$, the Fréchet derivative is defined as:

$$(\mathcal{K}'(R^*))w(t) := \int_0^t k^{(0,1)}(s, R^*(s))w(s)\, ds, \quad t \in \Omega_T, \tag{10}$$

where the kernel $k(t, R(t))$ is given by

$$k(t, R(t)) = \beta \left(N - \tilde{s}_0 e^{-\mu R(t)} - R(t)\right),$$

and its partial derivative with respect to R is computed as

$$k^{(0,1)}(t, R(t)) = \frac{\partial}{\partial R} k(t, R(t)) = \beta \left(\tilde{s}_0 \mu e^{-\mu R(t)} - 1\right),$$

leading to

$$k^{(0,1)}(t, R^*(t)) = \beta \left(\tilde{s}_0 \mu e^{-\mu R^*(t)} - 1\right).$$

To justify the validity of the Fréchet derivative, we first verify that the operator $\mathcal{K}$ is Gâteaux differentiable. For a fixed direction $w \in \mathbb{X}$, the Gâteaux derivative of $\mathcal{K}$ at R^* in the direction w is given by

$$\lim_{\epsilon \to 0} \frac{\mathcal{K}(R^* + \epsilon w)(t) - \mathcal{K}(R^*)(t)}{\epsilon} = \int_0^t k^{(0,1)}(s, R^*(s))w(s)\, ds,$$

provided the derivative $k^{(0,1)}(t, R(t))$ exists and is continuous in R, it follows that the operator $\mathcal{K}$ is Fréchet differentiable at R^*, and the expression in (10) defines its Fréchet derivative.

We now prove that $\mathcal{K}'(R^*)$ is bounded in $\mathbb{X}$. For all $w \in \mathbb{X}$, we have:

$$|(\mathcal{K}'(R^*))w(t)| = \left|\beta \int_0^t \left(\tilde{s}_0 \mu e^{-\mu R^*(s)} - 1\right) w(s)\, ds\right| \leq \beta \left(\tilde{s}_0\mu + 1\right) t \|w\|_\infty. \tag{11}$$

Taking the supremum over $t \in \Omega_T$, we obtain:

$$\|(\mathcal{K}'(R^*))w\|_\infty \leq \beta \left(\tilde{s}_0 + 1\right) T \|w\|_\infty. \tag{12}$$

This shows that $\mathcal{K}'(R^*)$ is a bounded linear operator with a norm proportional to $\beta \left(\tilde{s}_0 + 1\right) T$.

In the following, we establish the Lipschitz continuity of $\mathcal{K}'$. For any $R, S \in \mathbb{X}$, the difference $\mathcal{K}'(R) - \mathcal{K}'(S)$ satisfies:

$$\|(\mathcal{K}'(R) - \mathcal{K}'(S))w\|_\infty \leq \beta \left(\tilde{s}_0 + 1\right) T \|R - S\|_\infty \|w\|_\infty. \tag{13}$$

Letting $\mathcal{T}(R) := \mathcal{K}(R)(t) + \tilde{r}_0$, for all $R \in \mathbb{X}$, this implies

$$\mathcal{T}(R^*) = R^*. \tag{14}$$

2.1. Shifted third kind Chebyshev polynomials

We begin by recalling some fundamental definitions of the TKCPs, denoted by $V_n(x)$ for $n \geq 0$ and $x \in I = [-1, 1]$. These polynomials are defined by the three-term recurrence relation (see, e.g., [30,31]):

$$V_{n+1}(x) = 2xV_n(x) - V_{n-1}(x), \quad \text{for } n \geq 1, \tag{15}$$

with initial conditions

$$V_0(x) = 1, \quad V_1(x) = 2x - 1. \tag{16}$$

The polynomials $V_n(x)$ are orthogonal with respect to the weight function $\omega(x) = \sqrt{\frac{1+x}{1-x}}$ over the interval I. Their orthogonality condition is given by:

$$\int_{-1}^{1} V_m(x)V_n(x)\omega(x)\, dx = \pi\delta_{n,m}, \tag{17}$$

where $\delta_{n,m}$ is the Kronecker delta.

Consider the change of variable between $x \in I$ and $t \in \Omega_T = [0, T]$:

$$x = \frac{2t}{T} - 1 \quad \text{and} \quad t = \frac{T}{2}(x + 1). \tag{18}$$

Using this transformation, we define the shifted third-kind Chebyshev polynomials of degree n as:

$$\mathbb{T}_n(t) = V_n\left(\frac{2t}{T} - 1\right), \quad t \in \Omega_T. \tag{19}$$

Let $L^2_{\omega_T}(\Omega_T)$ denote the weighted Hilbert space, defined as:

$$L^2_{\omega_T}(\Omega_T) = \left\{R : \Omega_T \to \mathbb{R} \,\middle|\, R \text{ is measurable and } \|R\|_{\omega_T} < \infty\right\}, \tag{20}$$

where the inner product and norm are given by:

$$(R, S)_{\omega_T} = \int_0^T R(t)S(t)\omega_T(t)\, dt, \quad \|R\|_{\omega_T} = \sqrt{(R, R)_{\omega_T}}. \tag{21}$$

Here, the weight function is $\omega_T(t) = \sqrt{\frac{t}{T-t}}$. From (17) and (19), it follows that the shifted polynomials $\mathbb{T}_n(t)$ are orthogonal with respect to $\omega_T(t)$:

$$\int_0^T \mathbb{T}_m(t)\mathbb{T}_n(t)\omega_T(t)\, dt = \frac{\pi T}{2}\delta_{n,m}. \tag{22}$$

Moreover, the set $\{\mathbb{T}_n\}_{n=0}^\infty$ forms a complete orthogonal system in $L^2_{\omega_T}(\Omega_T)$.

We introduce the weighted orthogonal projection operator P_N^T, which maps the weighted Hilbert space $L^2_{\omega_T}(\Omega_T)$ onto the polynomial space $\mathbb{P}_N$. This operator is defined by the condition:

$$(P_N^T R - R, \phi)_{\omega_T} = 0, \quad \forall \phi \in \mathbb{P}_N. \tag{23}$$

Since $P_N^T R$ is a projection onto $\mathbb{P}_N$, it admits a finite expansion in terms of the basis $\{\mathbb{T}_n(t)\}_{n=0}^N$:

$$P_N^T R(t) = \sum_{n=0}^{N} R_{n,N}\mathbb{T}_n(t). \tag{24}$$

The expansion coefficients $R_{n,N}$ are uniquely determined by enforcing the orthogonality condition (24), which yields:

$$R_{n,N} = \frac{2}{\pi T}\int_0^T R(t)\mathbb{T}_n(t)\omega_T(t)\, dt. \tag{25}$$

Let $\{\xi_{i,N}^T, \omega_{i,N}^T\}_{i=0}^N$ denote the shifted third-kind Chebyshev–Gauss set, which are given by:

$$\xi_{i,N}^T = \frac{T}{2}(t_i + 1), \quad \omega_{i,N}^T = \frac{T}{2}\omega_{i,N}, \tag{26}$$

where $\{t_i, \omega_{i,N}\}_{i=0}^N$ are the third-kind Chebyshev–Gauss set. For all $\psi \in \mathbb{P}_{2N+1}$, we deduce

$$\begin{aligned}\int_0^T \psi(t)\omega_T(t)dt &= \frac{T}{2}\int_{-1}^{1} \psi(\frac{T}{2}(x+1))\omega(x)dx \\ &= \sum_{i=0}^{N} \psi(\frac{T}{2}(t_i+1))\frac{T}{2}\omega_{i,N} \\ &= \sum_{i=0}^{N} \psi(\xi_{i,N}^T)\omega_{i,N}^T.\end{aligned} \tag{27}$$

For notational convenience, we associate pairs of functions with the change of variable in (18) as follows:

$$R(t) = R\left(\frac{T}{2}(x + 1)\right) := R_T(x). \tag{28}$$

To estimate the error, we define the derivative operator:

$$D_t R := \frac{T}{2}\frac{dR}{dt}, \tag{29}$$

and by induction, we obtain:

$$D_t^k R := \left(\frac{T}{2}\right)^k \frac{d^k R}{dt^k} = \partial_x^k R_T, \quad k = 0, 1, \ldots. \tag{30}$$

Further, define

$$H_T^m(\Omega_T) = \{R : D_t^k R \in L^2_{\omega_T}(\Omega_T), \quad 0 \leq k \leq m\}, \tag{31}$$

with

$$|R|_{H_T^{m,N}} = \left(\sum_{k=\min\{m,N+1\}}^{m} \|D_t^k R\|^2_{L^2_{\omega_T}(\Omega_T)} \right)^{1/2}. \tag{32}$$

In the following lemma, we prove the convergence rates of the approximate solution to the exact solution.

Lemma 1. *Let $m \in \mathbb{N}^*$. For all $R \in H_T^m(\Omega_T)$, the following inequality holds:*

$$\|P_N^T R - R\|_\infty \le c N^{\frac{1}{2}-m} |R|_{H_T^{m,N}}. \tag{33}$$

where c is a positive constant independent of N and u, and N denotes the degree of the highest-order SCPs.

Proof. Let P_N be the projection operator associated with the third-kind Chebyshev polynomial. We have

$$\|P_N^T R - R\|_\infty = \|P_N R_T - R_T\|_\infty. \tag{34}$$

According to Lemma 1 in [32], for any $R_T \in H^m(I)$ with $m \ge 1$, it holds that

$$\|P_N R_T - R_T\|_\infty \le c N^{\frac{1}{2}-m} |R_T|_{H^{m,N}}. \tag{35}$$

Using (28) and (30), we obtain

$$\begin{aligned} \|D_t^k R\|^2_{L^2_{\omega_T}(\Omega_T)} &= \int_0^T |D_t^k R(t)|^2 \omega_T(t)\, dt = \int_{-1}^{1} |\partial_x^k R_T(x)|^2 \omega(x)\, dx \\ &= \|\partial_x^k R_T\|^2_{L^2_\omega(I)}. \end{aligned} \tag{36}$$

This implies that $|R|_{H_T^{m,N}} = |R_T|_{H^{m,N}}$. Hence, we conclude that

$$\|P_N^T R - R\|_\infty \le c N^{\frac{1}{2}-m} |R|_{H_T^{m,N}}. \tag{37}$$

Thus, the proof is complete.

3. Collocation method

In this section, we describe the collocation method associated with the shifted third-kind Chebyshev polynomials for solving Equation (3). First, we expand R using a finite series of shifted third-kind Chebyshev polynomials as follows:

$$R_N(x) = \sum_{n=0}^{N} R_{n,N}\, \mathbb{T}_n(t) = \mathbf{R}^T\, \mathbf{T}_N(t), \tag{38}$$

where

$$\mathbf{R} = \left(R_{0,N}, R_{1,N}, \dots, R_{N,N}\right)^{\mathrm{T}} \text{ and } \mathbf{T}_N(t) = \left(\mathbb{T}_0(t), \mathbb{T}_1(t), \dots, \mathbb{T}_N(t)\right)^{\mathrm{T}}. \tag{39}$$

Substituting (38) into (3), we obtain the residual function as follows:

$$r_N(t) = \mathbf{R}^T\, \mathbf{T}_N(t) - \int_0^t k\left(s, \mathbf{R}^T\, \mathbf{T}_N(s)\right) ds - \tilde{r}_0. \tag{40}$$

The residual function satisfies $r_N(\xi_{i,N}^T) = 0$ for all $i = 0, \dots, N$. Then,

$$\mathbf{R}^T\, \mathbf{T}_N(\xi_{i,N}^T) - \int_0^{\xi_{i,N}^T} k\left(s, \mathbf{R}^T\, \mathbf{T}_N(s)\right) ds - \tilde{r}_0 = 0. \tag{41}$$

To solve (41) in practice, the integrals appearing in these formulas must be evaluated numerically. For this purpose, we employ a numerical integration scheme based on the shifted third-kind Chebyshev–Gauss quadrature set $\{\xi_{i,N}^{\xi_{i,N}^T}, \omega_{i,N}^{\xi_{i,N}^T}\}_{i=0}^N$, where the nodes and weights are defined as:

$$\xi_{i,N}^{\xi_{i,N}^T} = \frac{\xi_{i,N}^T}{2}(t_i + 1), \quad \omega_{i,N}^{\xi_{i,N}^T} = \frac{\xi_{i,N}^T}{2}\omega_{i,N},$$

the integral is then approximated as:

$$\int_0^{\xi_{i,N}^T} \tilde{k}\left(s, \mathbf{R}^T\, \mathbf{T}_N(s)\right) \omega_{\xi_{i,N}^T}(t) ds \approx \sum_{j=0}^{N} \tilde{k}\left(\xi_{j,N}^{\xi_{i,N}^T}, \mathbf{R}^T\, \mathbf{T}_N(\xi_{j,N}^{\xi_{i,N}^T})\right) \omega_{j,N}^{\xi_{i,N}^T}, \tag{42}$$

where $\tilde{k}\left(t, \mathbf{R}^T\, \mathbf{T}_N(t)\right) = \sqrt{\frac{\xi_{i,N}^T - t}{t}}\, k\left(t, \mathbf{R}^T\, \mathbf{T}_N(t)\right)$. Let us denote

$$\begin{aligned} &\mathrm{K}(\mathbf{R}) = \tilde{k}\left(\xi_{j,N}^{\xi_{i,N}^T}, \mathbf{R}^T\, \mathbf{T}_N(\xi_{j,N}^{\xi_{i,N}^T})\right), \quad \mathrm{f} = (\tilde{r}_0, \dots, \tilde{r}_0)^{\mathrm{T}}, \\ &\mathrm{W} = \mathrm{diag}(\omega_{j,N}^{\xi_{i,N}^T}), \quad D_{N,i,j} = \mathbf{T}_N(\xi_{j,N}^{\xi_{i,N}^T}), \quad \mathrm{D} = (D_{N,i,j}). \end{aligned} \tag{43}$$

With these definitions, the system (41) simplifies to

$$\mathrm{Q}(\mathbf{R}) = \mathrm{D}\mathbf{R} - \mathrm{K}(\mathbf{R})\mathrm{W} - \mathrm{f} = 0. \tag{44}$$

The system (44) can be solved using the Newton–Raphson iteration method (NIM) as

$$\mathbf{R}^{(k+1)} = \mathbf{R}^{(k)} - [J_{\mathrm{Q}}(\mathbf{R}^{(k)})]^{-1} \mathrm{Q}(\mathbf{R}^{(k)}), \tag{45}$$

where $J_{\mathrm{Q}}(\mathbf{R})$ is the Jacobian matrix of $\mathrm{Q}(\mathbf{R})$, defined by

$$\left[J_{\mathrm{Q}}(\mathbf{R})\right]_{ij} = \frac{\partial Q_i(\mathbf{R})}{\partial R_{n,N}}. \tag{46}$$

3.1. Convergence of Newton's method

The Newton method converges quadratically under the following standard conditions:

- The function Q is Fréchet differentiable in a neighborhood of the exact solution $\mathbf{R}^*$.
- The Jacobian $J_{\mathrm{Q}}(\mathbf{R})$ is Lipschitz continuous near $\mathbf{R}^*$, i.e.,

$$\|J_Q(\mathbf{R}_1) - J_Q(\mathbf{R}_2)\| \le L\|\mathbf{R}_1 - \mathbf{R}_2\|. \tag{47}$$

- The Jacobian is invertible at $\mathbf{R}^*$ with bounded inverse, i.e., $\|J_Q^{-1}(\mathbf{R}^*)\| < \infty$.

Under these conditions, the Newton iteration satisfies the following quadratic convergence estimate:

$$\|\mathbf{R}^{(k+1)} - \mathbf{R}^*\| \le \kappa \|\mathbf{R}^{(k)} - \mathbf{R}^*\|^2, \quad \text{with} \quad \kappa = \frac{L}{2}\|J_Q^{-1}(\mathbf{R}^*)\|. \tag{48}$$

Furthermore, the convergence rate can be bounded as:

$$\limsup_{k\to\infty} \frac{\|\mathbf{R}^{(k+1)} - \mathbf{R}^*\|}{\|\mathbf{R}^{(k)} - \mathbf{R}^*\|^2} \le \gamma, \tag{49}$$

where $\gamma = \frac{\beta(\mu\tilde{s}_0+1)}{2\sigma_{\min}}$, with $\sigma_{\min}$ the smallest singular value of $J_Q(\mathbf{R}^*)$ and β a constant associated with the Lipschitz bound of the kernel function $k(t, R)$. This expression reflects how the nonlinearity of the integral term impacts convergence. In practice, we monitor convergence using the residual norm:

$$\frac{\|\mathrm{Q}(\mathbf{R}^{(k+1)})\|}{\|\mathrm{Q}(\mathbf{R}^{(k)})\|} \le \rho_k, \quad \text{with} \quad \rho_k \to 0 \quad \text{superlinearly}. \tag{50}$$

Thus, the Newton method efficiently resolves the nonlinearity in the collocation system through iterative linearization and, under appropriate regularity assumptions, guarantees fast (quadratic) convergence to the exact solution.

4. Convergence analysis

This section examines the existence, uniqueness and convergence of the approximate solution R_N for the following approximate Voltera integral equation

$$R_N = P_N^T \mathcal{T}(R_N). \tag{51}$$

To obtain a more accurate solution, we define the iterated solution as follows:

$$\widetilde{R}_N = \mathcal{T}(R_N). \tag{52}$$

Next, we define the operators $\mathcal{T}_N$ and $\widetilde{\mathcal{T}}_N$ on $\mathbb{X}$, mapping $\mathbb{X}$ onto itself, as follows:

$$\mathcal{T}_N R := P_N^T \mathcal{T}(R), \tag{53}$$

$$\widetilde{\mathcal{T}}_N R := \mathcal{T}(P_N^T R), \tag{54}$$

The above definitions satisfy the relations

$$\mathcal{T}_N R_N = R_N, \tag{55}$$

$$\widetilde{\mathcal{T}} \widetilde{R}_N = \widetilde{R}_N, \tag{56}$$

For any $w \in \mathbb{X}$, the Fréchet derivative of $\widetilde{\mathcal{T}}_N$ at R^* is given by

$$\widetilde{\mathcal{T}}_N'(R^*)w = T'(P_N^T R^*)w, \tag{57}$$

where

$$T'(R^*)w = \mathcal{K}'(R^*)w.$$

This theorem delineates the circumstances wherein the solvability of one equation directly implies the solvability of another, and for a rigorous treatment of the convergence properties of the approximate solution, we refer to Theorem 2 in [33].

Theorem 1. *Let $R^* \in \mathbb{X}$ be an isolated solution of Eq. (3). Assume that 1 is not an eigenvalue of the operator $\mathcal{T}'(R^*)$. Under this condition, Eq. (51) admits a unique solution $\widetilde{R}_N$ in the ball $\mathcal{B}(R^*, \delta) = \{R : \|R - R^*\|_\infty \le \delta\}$ for some $\delta > 0$ and sufficiently large N. Moreover, there exists a constant q, with $0 < q < 1$ and independent of N, such that the following error estimate holds:*

$$\frac{\rho_N}{1+q} \le \|\widetilde{R}_N - R^*\|_\infty \le \frac{\rho_N^T}{1-q}, \tag{58}$$

where

$$\rho_N^T = \left\| \left(I - \widetilde{\mathcal{T}}_N'(R^*)\right)^{-1} \left(\widetilde{\mathcal{T}}_N(R^*) - \mathcal{T}(R^*)\right) \right\|_\infty.$$

Additionally, the following bound holds for the error in the approximation solution R_N:

$$\|R^* - R_N\|_\infty = \mathcal{O}(N^{\frac{1}{2}-m}). \tag{59}$$

Proof. For any $w \in \mathbb{X}$, using Eq. (13), we have

$$\left\| \left(\widetilde{\mathcal{T}}_N'(R^*) - \mathcal{T}'(R^*)\right) w \right\|_\infty = \left\| \left(\mathcal{K}'(P_N^T R^*) - \mathcal{K}'(R^*)\right) w \right\|_\infty.$$

By the properties of $\mathcal{K}'$ and the given assumptions, it follows that

$$\left\| \left(\widetilde{\mathcal{T}}_N'(R^*) - \mathcal{T}'(R^*)\right) w \right\|_\infty \le \beta(\tilde{s}_0\mu + 1)T \|P_N^T R^* - R^*\|_\infty \|w\|_\infty.$$

From Lemma 1, we further obtain

$$\left\| \left(\widetilde{\mathcal{T}}_N'(R^*) - \mathcal{T}'(R^*)\right) w \right\|_\infty \le c\beta(\tilde{s}_0\mu + 1)T N^{\frac{3}{4}-m} |R|_{H_T^{m,N}} \|w\|_\infty.$$

This implies that

$$\left\| \widetilde{\mathcal{T}}_N'(R^*) - \mathcal{T}'(R^*) \right\|_\infty \to 0 \quad \text{as} \quad N \to \infty,$$

which shows that $\widetilde{\mathcal{T}}_N'(R^*)$ converges in norm to $\mathcal{T}'(R^*)$.

Moreover, since 1 is not an eigenvalue of $\mathcal{T}'(R^*)$, by Theorem 3.11 in [34, p. 55], the inverse operator $(I - \widetilde{\mathcal{T}}_N'(R^*))^{-1}$ exists and is uniformly bounded on $\mathbb{X}$ for sufficiently large N. Specifically, there exists a constant $M > 0$ such that

$$\left\| \left(I - \widetilde{\mathcal{T}}_N'(R^*)\right)^{-1} \right\|_\infty \le M < \infty.$$

Next, we estimate $\|\widetilde{\mathcal{T}}_N'(R^*) - \widetilde{\mathcal{T}}_N'(R)\|_\infty$ for any $R \in \mathcal{B}(R^*, \delta)$ and $R \in \mathbb{X}$. Using Eq. (13), we have

$$\left\| \left(\widetilde{\mathcal{T}}_N'(R^*) - \widetilde{\mathcal{T}}_N'(R)\right) w \right\|_\infty = \left\| \left(\mathcal{K}'(P_N^T R^*) - \mathcal{K}'(P_N^T R)\right) w \right\|_\infty.$$

From the properties of $\mathcal{K}'$, it follows that

$$\left\| \left(\widetilde{\mathcal{T}}_N'(R^*) - \widetilde{\mathcal{T}}_N'(R)\right) w \right\|_\infty \le \beta(\tilde{s}_0\mu + 1)T \|P_N^T R^* - P_N^T R\|_\infty \|w\|_\infty.$$

Since $\|P_N^T R^* - P_N^T R\|_\infty \le \|P_N^T\| \|R^* - R\|_\infty$, we obtain

$$\left\| \left(\widetilde{\mathcal{T}}_N'(R^*) - \widetilde{\mathcal{T}}_N'(R)\right) w \right\|_\infty \le \beta(\tilde{s}_0\mu + 1)T \|P_N^T\| \delta \|w\|_\infty.$$

This implies

$$\|\widetilde{\mathcal{T}}_N'(R^*) - \widetilde{\mathcal{T}}_N'(R)\|_\infty \le \beta(\tilde{s}_0\mu + 1)T \|P_N^T\| \delta.$$

Letting $\gamma_T = \|P_N^T\|$, we have

$$\sup_{\|R-R^*\|_\infty \le \delta} \|(I - \widetilde{\mathcal{T}}_N'(R^*))^{-1}(\widetilde{\mathcal{T}}_N'(R^*) - \widetilde{\mathcal{T}}_N'(R))\|_\infty \le M\beta(\tilde{s}_0\mu + 1)T\gamma_T\delta.$$

Let $q = M\beta(\tilde{s}_0\mu + 1)T\gamma_T\delta$ and choose δ sufficiently small such that $0 < q < 1$. This proves Eq. (4.4) of Theorem 2 in [33].

Using (9) and (33), we obtain

$$\rho_N^T = \|(I - \widetilde{\mathcal{T}}_N'(R^*))^{-1}(\widetilde{\mathcal{T}}(R^*) - \mathcal{T}(R^*))\|_\infty \le M\|\widetilde{\mathcal{T}}(R^*) - \mathcal{T}(R^*)\|_\infty.$$

Since $\widetilde{\mathcal{T}}(R^*) = \mathcal{K}(P_N^T R^*)$, it follows that

$$\rho_N^T \le M\|\mathcal{K}(P_N^T R^*) - \mathcal{K}(R^*)\|_\infty \le M\beta(\tilde{s}_0 + 1)T\|P_N^T R^* - R^*\|_\infty.$$

From Lemma 1, we have

$$\rho_N^T \le M\beta(\tilde{s}_0 + 1)Tc N^{\frac{1}{2}-m} |R^*|_{H_T^{m,N}} \to 0 \quad \text{as} \quad N \to \infty. \tag{60}$$

By choosing N large enough such that $\rho_N^T \le \delta(1-q)$, we satisfy Eq. (4.6) of Theorem 2 in [33]. Applying Theorem 2 of [33], we derive

$$\frac{\rho_N^T}{1+q} \le \|\widetilde{R}_N - R^*\|_\infty \le \frac{\rho_N^T}{1-q}. \tag{61}$$

Finally, we estimate the error between R_N and R^*, where $R_N = P_N^T \widetilde{R}_N$. The error can be expressed as

$$R^* - R_N = R^* - P_N^T \widetilde{R}_N = (R^* - P_N^T R^*) + (P_N^T R^* - P_N^T \widetilde{R}_N).$$

This leads to the inequality

$$\|R^* - R_N\|_\infty \le \|R^* - P_N^T R^*\|_\infty + \|P_N^T\|_\infty \|R^* - \widetilde{R}_N\|_\infty.$$

Using the results from (33), (60) and (61), we obtain

$$\|R^* - R_N\|_\infty \le \left(\frac{\gamma_T M\beta(\tilde{s}_0 + 1)T}{1-q} + 1\right) c N^{\frac{1}{2}-m} |R^*|_{H_T^{m,N}}. \tag{62}$$

This completes the proof.

We can now effectively estimate the error between the approximate solutions S_N and I_N, and the target solutions S^* and I^*, respectively, in the $\mathbb{X}$ space. The following definitions hold:

$$S_N(t) = \tilde{s}_0 e^{-\mu R_N(t)}, \tag{63}$$

$$I_N(t) = N - \tilde{s}_0 e^{-\mu R_N(t)} - R_N(t). \tag{64}$$

Theorem 2. *Let S^*, I^*, R^* denote the solutions of the system (1). Then, the errors between S^* and S_N, as well as I^* and I_N, are bounded as follows:*

$$\|S^* - S_N\|_\infty = \mathcal{O}(N^{\frac{1}{2}-m}), \tag{65}$$

and

$$\|I^* - I_N\|_\infty = \mathcal{O}(N^{\frac{1}{2}-m}). \tag{66}$$

Proof. Using Eqs. (5), (6), (63), (64), and (59), we derive the following bounds:

For S_N:

$$\|S^* - S_N\|_\infty = \tilde{s}_0 \|e^{-\mu R^*(t)} - e^{-\mu R_N(t)}\|_\infty \le \tilde{s}_0\mu \|R^* - R_N\|_\infty. \tag{67}$$

For I_N:

$$\begin{aligned} \|I^* - I_N\|_\infty &= \beta\|\tilde{s}_0(e^{-\mu R^*(t)} - e^{-\mu R_N(t)}) + R^* - R_N\|_\infty \\ &\le \beta(\tilde{s}_0\mu + 1)\|R^* - R_N\|_\infty. \end{aligned} \tag{68}$$

Since $\|R^* - R_N\|_\infty = \mathcal{O}(N^{\frac{1}{2}-m})$, the bounds for $\|S^* - S_N\|_\infty$ and $\|I^* - I_N\|_\infty$ follow directly.

This concludes the proof.

Table 1
Comparison of S at different values of t with $N = 10$ for Test 1, including relative errors.

t	Our method	$R^T_{N,S}(t)$	Analytical solution	Method in [14]	Method in [35]
0	20.000000000000000	0.0	20.000000000000000	20.000000000000000	20.000000000000000
0.1	19.699578126359828	5.07e−16	19.699578126359818	19.699578126359821	19.699578126371996
0.2	19.398425570548401	9.27e−16	19.398425570548383	19.398425570548394	19.398425571303918
0.3	19.096713014982857	1.31e−15	19.096713014982832	19.096713014982853	19.096713023320397
0.4	18.794612274799267	2.08e−15	18.794612274799228	18.794612274799260	18.794612320125442
0.5	18.492295901674989	2.27e−15	18.492295901674947	18.492295901674989	18.492296068742188
0.6	18.189936784338556	3.30e−15	18.189936784338496	18.189936784338553	18.189937265652560
0.7	17.887707747739274	3.98e−15	17.887707747739203	17.887707747739270	17.887708916936980
0.8	17.585781152859408	5.06e−15	17.585781152859319	17.585781152859397	17.585783658414083
0.9	17.284328499144522	5.55e−15	17.284328499144426	17.284328499144518	17.284333375780378
1	16.983520031504586	6.42e−15	16.983520031504479	16.983520031504579	16.983528824749996
CPU	0.06				

5. Numerical results and discussion

In this section, we present a numerical solution to the SIR model using the proposed shifted Chebyshev method. The solution is illustrated through detailed figures and tables. We analyze the system of Eqs. (1) by exploring various values of the parameters M, α, and β, as well as the initial conditions $\tilde{s}_0$, $\tilde{i}_0$, and $\tilde{r}_0$. Also, we denote

$$e^T_{N,S} = \|S_{256} - S_N\|_\infty = \sup_{t\in\Omega_T} |S_{256}(t) - S_N(t)| \qquad R^T_{N,S}(t) = \frac{|S(t) - S_N(t)|}{|S(t)|},$$

$$e^T_{N,I} = \|I_{256} - I_N\|_\infty = \sup_{t\in\Omega_T} |I_{256}(t) - I_N(t)| \qquad R^T_{N,S}(t) = \frac{|I(t) - I_N(t)|}{|I(t)|},$$

$$e^T_{N,R} = \|R_{256} - R_N\|_{\infty=\sup_{t\in\Omega_T}|R_{256}(t)-R_N(t)|} \qquad R^T_{N,S}(t) = \frac{|R(t) - R_N(t)|}{|R(t)|},$$

where S_{256}, I_{256} and R_{256} are the reference solutions obtained using a high-resolution collocation method with $N = 256$. The computations were carried out in MATLAB on a system equipped with an Intel® Core™ i3-5010U CPU @ 2.10 GHz and 4 GB of RAM. The CPU times (in seconds) for different values of N are reported.

Test 1. *In this test, we apply the shifted Chebyshev method presented in Section 3 with different values of N and T to compute the numerical solution of a system where S represents the number of susceptible individuals, I represents the number of infected individuals, and R represents the number of recovered individuals. The initial population values are $S(0) = 20$, $I(0) = 15$, and $R(0) = 10$. The infection rate is $\alpha = 0.01$, and the susceptibility rate is $\beta = 0.02$.*

In Tables 1–3, we present the numerical values of S, I, and R and relative errors obtained by applying our method with $N = 10$ and $T = 1$ at different time points t. These results are compared with those from [14,35]. Additionally, in Table 4, we display the maximum errors obtained by our method compared to those in [14] at $t = 0, 0.2, 0.4, 0.6, 0.8$, and 1.

Furthermore, in Fig. 1, the approximate solutions are plotted for $N = 10$ in the interval $[0, 1]$ (see Fig. 1(a)) and for $N = 32$ in the interval $[0, 365]$ (see Fig. 1(b)). The obtained results confirm that our method provides accurate solutions and performs well even over large time intervals.

Test 2. *In this test, we set the infection rate to $\alpha = 0.05$ and the susceptibility rate to $\beta = 0.06$. With these parameters, we obtain the reciprocal relative removal rate as*

$$\mu = \frac{\alpha}{\beta} = \frac{5}{6}.$$

The initial population values are $S(0) = 20$, $I(0) = 15$, and $R(0) = 5$ for the first case, while $R(0) = 0$ for the second case, as described in [14]. The problem was solved numerically for two scenarios: (1) $T = 1$ with $R(0) = 5$ and (2) $T = 5$ with $R(0) = 0$. The method proposed in [14] yields accurate results for $T = 1$ but performs poorly for $T = 5$.

By applying our method, we compute the L^∞-errors of the differences between S_{256} and S_N, I_{256} and I_N, and R_{256} and R_N for $R(0) = 5$ and $R(0) = 0$, as summarized in Tables 6 and 7, respectively. The computations are performed for $T = 1, 10, 50$ and 100 with different values of $N = 8, 16, 32, 64$ and 128. Additionally, Table 5 provides the values of the maximum of I_N and the absolute error between I_N and the theoretical maximum $I_{\max}$, where

$$I_{\max} = -\frac{6}{5}\ln\left(\frac{5}{6}\right) + 35 - \frac{6}{5}\ln(20) \approx 30.423907139887959.$$

The approximate solutions are plotted in Fig. 2 for $R(0) = 5$, with $N = 10$ over the interval $[0, 1]$ (see Fig. 2(a)) and $N = 128$ over the interval $[0, 100]$ (see Fig. 2(b)). Similarly, Fig. 3 shows the results for $R(0) = 0$, with $N = 10$ over $[0, 1]$ (see Fig. 3(a)) and $N = 128$ over $[0, 100]$ (see Fig. 3(b)).

The obtained results demonstrate that our method is accurate for both small and large intervals, outperforming the reference method in [14] for the case of $T = 5$.

Test 3. *In this test, we set the infection rate to $\alpha = 0.0004$ and the susceptibility rate to $\beta = 0.02$. With these parameters, we obtain a reciprocal relative removal rate of $\mu = \frac{\alpha}{\beta} = 0.02$. The initial population values are $S(0) = 998$, $I(0) = 2$, and $R(0) = 0$. In [15], this problem was numerically solved for $T = 365$ days using the method described in the same reference. The results showed a maximum infected population of $I_{\max} = 800$, with the peak occurring on day 25, where time is measured in days. The study also provided results for $T = 365$ days.*

Here, by applying our method, we compute the L^∞-errors of the differences between S_{256} and S_N, I_{256} and I_N, and R_{256} and R_N, as summarized in Table 6. Additionally, Table 9 provides the values of the maximum of I_N and the absolute error between I_N and the theoretical maximum $I_{\max}$, where

$$I_{\max} = -50\ln(0.02) + 1000 - 50\ln(998) \approx 800.3134864558341.$$

This theoretical value serves as a benchmark for evaluating the accuracy of our numerical results.

Furthermore, the approximate solutions are plotted in Fig. 2, where I_N is shown to reach its maximum value at a peak day $t_p \approx 24.5194$ for $N = 128$ and $T = 40$ (see Fig. 4(a)). The graphs of S, I, and R over the interval $[0, 365]$ are also provided (see Fig. 4(b)). The obtained results demonstrate that our method is highly accurate more than the results in [15], particularly in predicting the maximum value of I and the peak day. This accuracy holds consistently across both small and large time intervals, confirming the robustness of our approach.

Stability analysis

An essential aspect of any numerical method is its stability with respect to perturbations in data and discretization parameters. In the context of the proposed shifted Chebyshev spectral collocation method, we observed stable behavior across all test scenarios, including long-time integrations and high-resolution discretizations. The numerical

Table 2
Comparison of I at different values of t with $N = 10$ for Test 1, including relative errors.

t	Our method	$R^T_{N,I}(t)$	Analytical solution	Method in [14]	Method in [35]
0	15.000000000000000	0.0	15.000000000000000	15.000000000000000	15.000000000000000
0.1	15.270151767750288	0.0	15.270151767750288	15.270151767750292	15.270151767739135
0.2	15.540493695580903	5.79e−16	15.540493695580912	15.540493695580912	15.540493694892319
0.3	15.810854891481981	5.69e−16	15.810854891481990	15.810854891481988	15.810854883914805
0.4	16.081063673364721	1.12e−15	16.081063673364739	16.081063673364731	16.081063632394240
0.5	16.350947966422424	1.35e−15	16.350947966422446	16.350947966422435	16.350947816046876
0.6	16.620335703006457	1.32e−15	16.620335703006479	16.620335703006461	16.620335271713763
0.7	16.889055223041751	1.89e−15	16.889055223041783	16.889055223041758	16.889054180356947
0.8	17.156935673000223	1.86e−15	17.156935673000255	17.156935673000223	17.156933450055682
0.9	17.423807401460902	2.82e−15	17.423807401460952	17.423807401460913	17.423803099002612
1	17.689502349313514	3.00e−15	17.689502349313567	17.689502349313525	17.689494638499998
CPU	0.06				

Table 3
Comparison of R at different values of t with $N = 10$ for Test 1, including relative errors.

t	Our method	$R^T_{N,R}(t)$	Analytical solution	Method in [14]	Method in [35]
0	10.000000000000000	0.0	10.000000000000000	10.000000000000000	10.000000000000000
0.1	10.030270105889889	2.99e−16	10.030270105889892	10.030270105889885	10.030539859150000
0.2	10.061080733870693	1.19e−15	10.061080733870705	10.061080733870693	10.062158873200000
0.3	10.092432093535159	1.78e−15	10.092432093535177	10.092432093535157	10.094856197050001
0.4	10.124324051836009	2.27e−15	10.124324051836032	10.124324051836007	10.128630985599999
0.5	10.156756131902576	2.95e−15	10.156756131902606	10.156756131902574	10.163482393750002
0.6	10.189727512654991	3.24e−15	10.189727512655024	10.189727512654985	10.199409576399999
0.7	10.223237029218968	4.31e−15	10.223237029219012	10.223237029218968	10.236411688450001
0.8	10.257283174140378	4.48e−15	10.257283174140424	10.257283174140372	10.274487884800001
0.9	10.291864099394569	5.24e−15	10.291864099394623	10.291864099394564	10.313637320349999
1	10.326977619181896	5.73e−15	10.326977619181955	10.326977619181891	10.353859150000002
CPU	0.06				

Table 4
The L^∞−errors for Test 1 with $T = 1$.

N	$\|S_N - S^*\|_\infty$		$\|I_N - I^*\|_\infty$		$\|R_N - R^*\|_\infty$		
	Our method	[14]	Our method	[14]	Our method	[14]	CPU
7	1.172e−12	2.202e−12	1.3074e−12	1.044e−11	1.7764e−13	2.065e−12	0.05
10	1.065e−13	9.948e−13	4.9738e−14	9.947e−14	5.8620e−14	6.394e−14	0.09

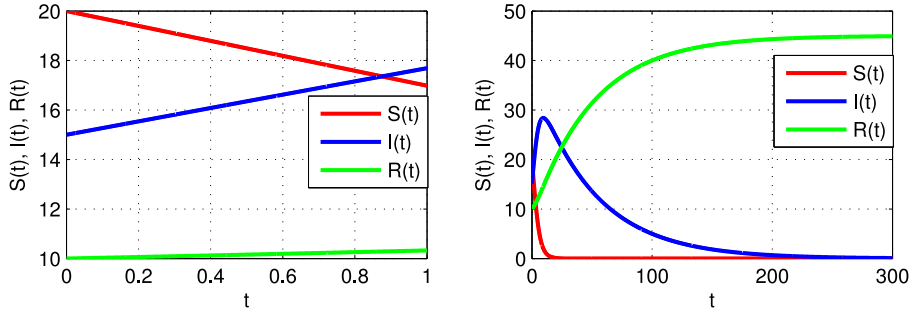

(a) $N = 10$ and $T = 1$. (b) $N = 128$ and $T = 300$.

Fig. 1. Graphical representation of the shifted Chebyshev approximate solution of S, I and R.

Table 5
The maximum value of I_N for Test 3.

N	$S(0) = 20$, $I(0) = 15$, and $R(0) = 5$			$S(0) = 20$, $I(0) = 15$, and $R(0) = 0$		
	$I_{N,\max}$	$\|I_{N,\max} - I_{\max}\|$	CPU	$I_{N,\max}$	$\|I_{N,\max} - I_{\max}\|$	CPU
8	30.42391082069724	3.68e−06	0.08	30.42391082069724	3.68e−06	0.09
16	30.42390715028353	1.04e−08	0.20	30.42390715028353	1.04e−08	0.19
32	30.42390713987995	8.00e−12	0.95	30.42390713987995	8.00e−12	0.57
64	30.42390713987995	8.00e−12	1.86	30.42390713987995	8.00e−12	1.98

results displayed in Tables 1–9 and Figs. 1–4 confirm this: the computed solutions remain bounded and accurate even for large final times (e.g., $T = 100$), and increasing the number of collocation points N leads to consistent improvement in accuracy without introducing numerical oscillations or divergence. Furthermore, the exponential decay of the L^∞-errors with respect to N, as presented in Tables 4–9, illustrates the spectral convergence of the method. Such behavior is a strong indicator of both the stability and efficiency of the scheme. These

Table 6
The $L^{\infty}-$errors for Test 2 with $S(0) = 20$, $I(0) = 15$ and $R(0) = 5$.

N	$T = 1$				$T = 10$			
	$e^T_{N,S}$	$e^T_{N,I}$	$e^T_{N,R}$	CPU	$e^T_{N,S}$	$e^T_{N,I}$	$e^T_{N,R}$	CPU
8	4.99e−07	4.88e−07	1.51e−08	0.05	4.40e−01			0.05
16	1.05e−13	1.10e−13	1.78e−15	0.20	1.25e−03	1.25e−03	1.17e−04	0.11
32	7.11e−15	7.11e−15	1.78e−15	0.30	8.78e−08	8.95e−08	1.23e−09	0.31
64	7.11e−15	1.07e−14	4.44e−15	1.10	2.13e−14	2.49e−14	1.07e−14	1.01
128	1.07e−14	1.24e−14	4.44e−15	3.40	1.42e−14	2.13e−14	1.07e−14	3.75
N	$T = 50$				$T = 100$			
	$e^T_{N,S}$	$e^T_{N,I}$	$e^T_{N,R}$	CPU	$e^T_{N,S}$	$e^T_{N,I}$	$e^T_{N,R}$	CPU
8								
16	8.97e−01			0.16			9.05e−01	0.10
32	2.62e−03	3.03e−03	4.81e−04	0.29	6.52e−02	5.01e−02	1.47e−02	0.28
64	9.98e−07	1.09e−06	3.70e−08	0.97	8.83e−05	9.45e−05	4.93e−06	1.02
128	6.13e−14	7.82e−14	2.84e−14	3.84	6.06e−10	6.38e−10	9.54e−12	3.86

Table 7
The $L^{\infty}-$errors for Test 2 with $S(0) = 20$, $I(0) = 15$ and $R(0) = 0$.

N	$T = 1$				$T = 10$			
	$e^T_{N,S}$	$e^T_{N,I}$	$e^T_{N,R}$	CPU	$e^T_{N,S}$	$e^T_{N,I}$	$e^T_{N,R}$	CPU
8	4.99e−07	4.88e−07	1.51e−08	0.06	4.40e−01		9.09e−01	0.05
16	1.05e−13	1.10e−13	6.66e−16	0.10	1.25e−03	1.25e−03	1.17e−04	0.10
32	7.11e−15	5.33e−15	1.33e−15	0.31	8.78e−08	8.95e−08	1.23e−09	0.29
64	1.07e−14	1.07e−14	1.55e−15	1.03	1.07e−14	2.13e−14	1.24e−14	1.01
128	7.11e−15	7.11e−14	4.44e−16	3.68	1.42e−14	2.84e−14	7.11e−15	3.66
N	$T = 50$				$T = 100$			
	$e^T_{N,S}$	$e^T_{N,I}$	$e^T_{N,R}$	CPU	$e^T_{N,S}$	$e^T_{N,I}$	$e^T_{N,R}$	CPU
8								
16	8.97e−01			0.11			9.05e−01	0.10
32	2.62e−03	3.03e−03	4.81e−04	0.31	6.52e−02	5.01e−02	1.47e−02	0.30
64	9.98e−07	1.09e−06	3.70e−08	1.04	8.83e−05	9.45e−05	4.93e−06	0.96
128	5.68e−14	7.82e−14	2.13e−14	3.78	6.06e−10	6.38e−10	9.51e−12	3.76

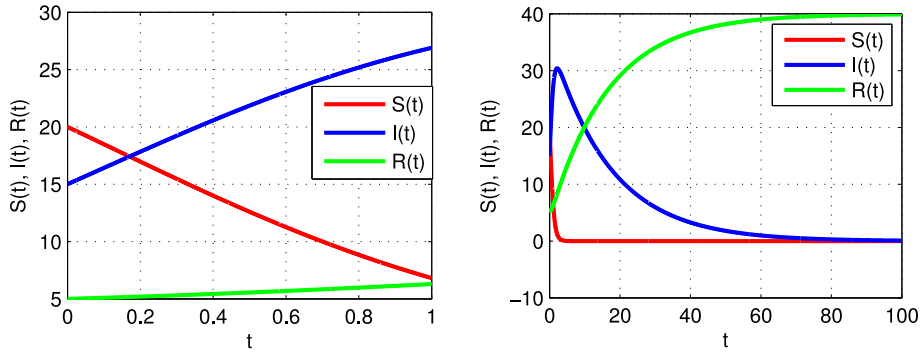

(a) $N = 10$ and $T = 1$. (b) $N = 128$ and $T = 100$.

Fig. 2. Graphical representation of the shifted Chebyshev approximate solution of S, I and R.

results highlight the robustness and numerical stability of the proposed scheme under varying initial conditions and parameter regimes.

6. Conclusion

In this work, we presented an efficient and accurate numerical approach based on the SCP collocation method for solving the biological SIR system modeling COVID-19. The proposed technique transforms the original problem into a nonlinear Volterra integral equation, which is then approximated using SCPs. Rigorous analysis established the method's convergence rate in the L^{∞}-norm as $\mathcal{O}(N^{-\frac{1}{2}-m})$, where N is

Table 8
The maximum values of I_N for Test 3.

N	$I_{N,\max}$	$\lvert I_{N,\max} - I_{\max}\rvert$	CPU
16	800.3021393820854	1.13e−02	0.18
32	800.3134864657228	9.89e−09	0.54
64	800.3134864558305	3.64e−12	1.62
128	800.3134864558304	3.64e−12	6.96

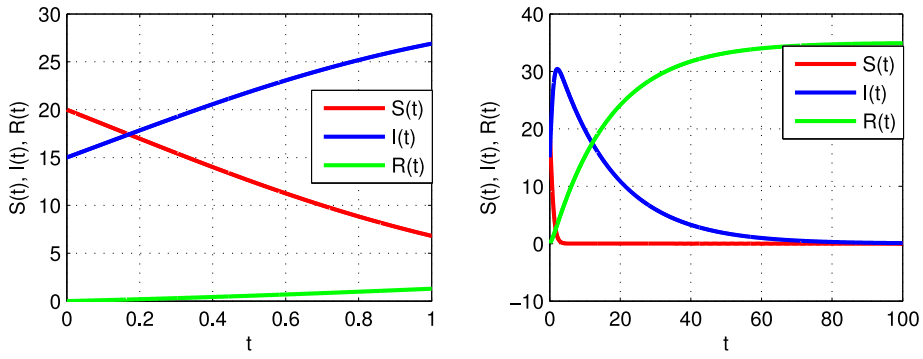

(a) $N = 10$ and $T = 1$. (b) $N = 128$ and $T = 100$.

Fig. 3. Graphical representation of the shifted Chebyshev approximate solution of S, I and R.

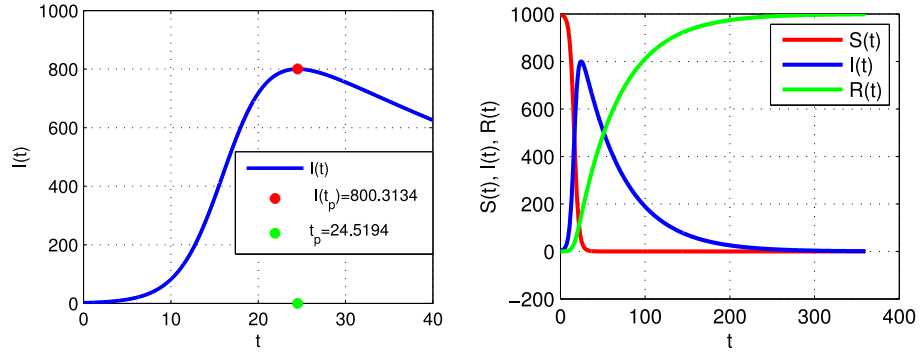

(a) $N = 128$ and $T = 40$. (b) $N = 128$ and $T = 360$.

Fig. 4. Graphical representation of the shifted Chebyshev approximate solution of S, I and R.

Table 9
The L^∞−errors for Test 3.

N	$T = 1$				$T = 10$			
	$e^T_{N,S}$	$e^T_{N,I}$	$e^T_{N,R}$	CPU	$e^T_{N,S}$	$e^T_{N,I}$	$e^T_{N,R}$	CPU
8	1.14e−13	2.13e−14	1.36e−14	0.04	1.63e−03	1.55e−03	8.40e−05	0.04
16	1.14e−13	7.11e−15	4.49e−15	0.10	7.24e−10	7.12e−10	3.48e−11	0.11
32	1.14e−13	5.46e−14	3.80e−14	0.43	5.68e−13	3.55e−13	6.93e−14	0.31
64	1.14e−13	5.77e−15	3.77e−15	1.16	4.55e−13	2.70e−13	2.80e−14	1.03
128	1.14e−13	4.88e−15	2.49e−15	3.95	1.36e−12	1.22e−12	4.09e−14	3.98
N	$T = 100$				$T = 200$			
	$e^T_{N,S}$	$e^T_{N,I}$	$e^T_{N,R}$	CPU	$e^T_{N,S}$	$e^T_{N,I}$	$e^T_{N,R}$	CPU
8								
16								
32								
64	1.21e−03	1.12e−03	1.28e−04	1.01			3.57e−01	1.10
128	3.85e−10	3.83e−10	5.81e−12	4.25	4.54e−06	4.53e−06	1.43e−07	4.15

the degree of the highest polynomial used and m reflects the smoothness of the solution.

Through extensive numerical experiments, we demonstrated that the method outperforms existing schemes in both accuracy and computational efficiency. Notably, it successfully captures key epidemiological behaviors, such as the timing and magnitude of the infection peak, as well as the long-term decline in the infected population. For example, in Test 2, the computed maximum infected population $I_{\max}$ aligned precisely with theoretical predictions, underscoring the method's reliability for critical decision-making during outbreaks.

Furthermore, the method remains robust over large time intervals (e.g., $T = 100$), making it particularly valuable for long-term epidemic forecasting and evaluating intervention strategies. Its sensitivity to parameters α and β also provides crucial insights into how transmission and recovery rates influence disease dynamics. These results highlight the method's dual utility: as a high-precision computational tool and as a practical framework for public health modeling.

Overall, the shifted Chebyshev collocation method provides a versatile and powerful approach for solving complex epidemic systems, combining rigorous theoretical foundations with practical applicability in real-world scenarios. Future research could explore its application to stochastic and multi dimensional fractional-order models, such as those analyzing the transmission dynamics of the COVID-19 pandemic, as discussed in [36,37].

CRediT authorship contribution statement

Walid Remili: Writing – review & editing, Writing – original draft, Visualization, Validation, Supervision, Resources, Methodology, Investigation, Funding acquisition, Formal analysis, Conceptualization. **Wen-Xiu Ma:** Writing – review & editing, Visualization, Supervision, Formal analysis, Conceptualization.

Declaration of competing interest

The authors declare that there are no financial, personal, or professional conflicts of interest that could influence the work presented in this manuscript. The authors research and findings have been conducted with the highest standards of academic integrity, free from any undue influence or bias.

Should any potential conflicts of interest arise in the future, the authors commit to disclosing them promptly to the editorial office and will take all necessary steps to maintain transparency and uphold ethical standards in our publication.

Data availability

No data was used for the research described in the article.

References

[1] N.A. Kudryashov, M.A. Chmykhov, M. Vigdorowitsch, Analytical features of the SIR model and their applications to COVID-19, Appl. Math. Model. 90 (2021) 466–473.

[2] D.J. Earn, J. Dushoff, S.A. Levin, Ecology and evolution of the flu, Trends Ecol. Evolut. 17 (7) (2002) 334–340.

[3] A. Khaleque, P. Sen, An empirical analysis of the Ebola outbreak in West Africa, Sci. Rep. 7 (1) (2017) 42594.

[4] W.O. Kermack, A.G. McKendrick, A contribution to the mathematical theory of epidemics, Proc. R. Soc. Lond. Ser. A Containing Pap. A Math. Phys. Character 115 (772) (1927) 700–721.

[5] T. Harko, F.S. Lobo, M.K. Mak, Exact analytical solutions of the susceptible-infected-recovered (SIR) epidemic model and of the SIR model with equal death and birth rates, Appl. Math. Comput. 236 (2014) 184–194.

[6] N.S. Barlow, S.J. Weinstein, Accurate closed-form solution of the SIR epidemic model, Phys. D: Nonlinear Phenom. 408 (2020) 132540.

[7] D. Prodanov, Comments on some analytical and numerical aspects of the SIR model, Appl. Math. Model. 95 (2021) 236–243.

[8] O.D. Makinde, Adomian decomposition approach to a SIR epidemic model with constant vaccination strategy, Appl. Math. Comput. 184 (2) (2007) 842–848.

[9] Y. Chakir, Global approximate solution of SIR epidemic model with constant vaccination strategy, Chaos Solitons Fractals 169 (2023) 113323.

[10] W. Piyawong, E.H. Twizell, A.B. Gumel, An unconditionally convergent finite-difference scheme for the SIR model, Appl. Math. Comput. 146 (2–3) (2003) 611–625.

[11] D. Conte, G. Pagano, B. Paternoster, N. Guarino, Positivity-preserving and elementary stable nonstandard method for a COVID-19 SIR model, Dolomites Res. Not. Approx. 15 (DRNA Volume 15.5) (2022) 65–77.

[12] R.E. Mickens, Numerical integration of population models satisfying conservation laws: NSFD methods, J. Biol. Dyn. 1 (4) (2007) 427–436.

[13] D. Baleanu, M.H. Abadi, A. Jajarmi, K.Z. Vahid, J. Nieto, A new comparative study on the general fractional model of COVID-19 with isolation and quarantine effects, Alex. Eng. J. 61 (6) (2022) 4779–4791.

[14] M. Kumar, et al., Spreading behavior of biological SIR system of a COVID-19 disease through a fast Taylor wavelet based numerical algorithm, Results Control. Optim. 13 (2023) 100316.

[15] V.A. Khoa, P.M. Quan, K.W. Blayneh, et al., Efficient relaxation scheme for the SIR and related compartmental models, J. Comput. Sci. 84 (2025) 102478.

[16] H. Srivastava, K.M. Saad, M. Khader, An efficient spectral collocation method for the dynamic simulation of the fractional epidemiological model of the Ebola virus, Chaos Solitons Fractals 140 (2020) 110174.

[17] N. Sriwastav, A.K. Barnwal, H. Ramos Calle, R.P. Agarwal, M. Singh, et al., New approach based on collocation and shifted chebyshev polynomials for a class of three-point singular BVPS, J. Appl. Anal. Comput. 13 (4) (2023) 2162–2183.

[18] S. Sayed, A. Mohamed, E. Abo-Eldahab, Y. Youssri, Spectral framework using modified shifted Chebyshev polynomials of the third-kind for numerical solutions of one-and two-dimensional hyperbolic telegraph equations, Bound. Value Probl. 2025 (1) (2025) 7.

[19] M. Abdelhakem, D. Abdelhamied, M. El-Kady, Y. Youssri, Two modified shifted Chebyshev–Galerkin operational matrix methods for even-order partial boundary value problems, Bound. Value Probl. 2025 (1) (2025) 34.

[20] Y.H. Youssri, A.G. Atta, M.O. Moustafa, Z. Waar, Explicit collocation algorithm for the nonlinear fractional Duffing equation via third-kind Chebyshev polynomials, Iran. J. Numer. Anal. Optim. 15 (2) (2025).

[21] Y. Youssri, L.A. Alnaser, A. Atta, A spectral collocation approach for time-fractional Korteweg–de Vries–Burgers equation via first-kind Chebyshev polynomials, Contemp. Math. (2025) 1501–1519.

[22] Y. Youssri, A. Atta, Adopted Chebyshev collocation algorithm for modeling human corneal shape via the Caputo fractional derivative, Contemp. Math. (2025) 1223–1238.

[23] Y. Youssri, A. Atta, Chebyshev Petrov–Galerkin method for nonlinear time-fractional integro-differential equations with a mildly singular kernel: YH Youssri, AG Atta, J. Appl. Math. Comput. 71 (3) (2025) 3891–3911.

[24] N. Sriwastav, A. Das, O. Shardt, J. Kumar, M. Singh, A meshfree approach for the rennet-induced coagulation equation: Spline based multistage Bernstein collocation method and its convergence analysis, Appl. Math. Model. 143 (2025) 116035.

[25] P. Pathak, A.K. Barnwal, N. Sriwastav, R. Singh, M. Singh, An algorithm based on homotopy perturbation theory and its mathematical analysis for singular nonlinear system of boundary value problems, Math. Methods Appl. Sci. 48 (7) (2025) 7745–7766.

[26] N. Sriwastav, R. N Prajapati, A. Singh, A.K. Barnwal, C. Cattani, M. Singh, A robust Legendre collocation scheme and convergence analysis for Lane–Emden multi-pantograph delay differential equations arising in stellar physics including Chandrasekhar's white dwarf problem, Numer. Algorithms (2025) 1–30.

[27] R. Singh, H. Garg, V. Guleria, Haar wavelet collocation method for Lane–Emden equations with Dirichlet, Neumann and Neumann–Robin boundary conditions, J. Comput. Appl. Math. 346 (2019) 150–161.

[28] N. Saha, R. Singh, Numerical algorithm for solving third-order Emden–Fowler type pantograph differential equations: Taylor operational matrix method, Soft Comput. (2025) 1–17.

[29] J. Shahni, R. Singh, C. Cattani, An efficient numerical approach for solving three-point Lane–Emden–Fowler boundary value problem, Math. Comput. Simulation 210 (2023) 1–16.

[30] J.C. Mason, D.C. Handscomb, Chebyshev Polynomials, Chapman and Hall/CRC, 2002.

[31] M.A. Snyder, Chebyshev Methods in Numerical Approximation, in: Prentice-Hall Series in Automatic Computation, Prentice-Hall, 1966, URL https://cir.nii.ac.jp/crid/1130000795738088832.

[32] E.H. Doha, M.A. Abdelkawy, A.Z. Amin, D. Baleanu, Shifted Jacobi spectral collocation method with convergence analysis for solving integro-differential equations and system of integro-differential equations, Nonlinear Anal. Model. Control 24 (3) (2019) 332–352.

[33] G.M. Vainikko, Galerkin's perturbation method and the general theory of approximate methods for nonlinear equations, USSR Comput. Math. Math. Phys. 7 (4) (1967) 1–41, http://dx.doi.org/10.1016/0041-5553(67)90140-1.

[34] K.E. Atkinson, The Numerical Solution of Integral Equations of the Second Kind, Reissue ed., in: Cambridge Monographs on Applied and Computational Mathematics 4, Cambridge University Press, 2009, URL http://gen.lib.rus.ec/book/index.php?md5=090763d9bd0216680cf125989c68d5f8.

[35] Q. Lin, S. Zhao, D. Gao, Y. Lou, S. Yang, S.S. Musa, M.H. Wang, Y. Cai, W. Wang, L. Yang, et al., A conceptual model for the coronavirus disease 2019 (COVID-19) outbreak in Wuhan, China with individual reaction and governmental action, Int. J. Infect. Dis. 93 (2020) 211–216.

[36] A.W. Tesfaye, T.S. Satana, Stochastic model of the transmission dynamics of COVID-19 pandemic, Adv. Difference Equ. 2021 (1) (2021) 457.

[37] W.-J. Zhu, S.-F. Shen, W.-X. Ma, A (2+ 1)-dimensional fractional-order epidemic model with pulse jumps for omicron COVID-19 transmission and its numerical simulation, Mathematics 10 (14) (2022) 2517.